Stepwise martensitic transformation in tool steel during laser powder bed fusion revealed by operando X-ray diffraction

Additive Manufacturing 127 (2026) 105323

Contents lists available at ScienceDirect

Additive Manufacturing

journal homepage: www.elsevier.com/locate/addma

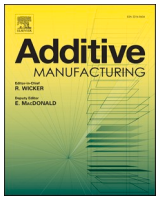

Stepwise martensitic transformation in tool steel during laser powder bed fusion revealed by operando X-ray diffraction

Huayue Zhang [a,*], Andaç Özsoy [b], Gowtham Soundarapandiyan [c,d], Malgorzata Grazyna Makowska [e], Pedro E.J. Rivera-Diaz-del-Castillo [f], Steven Van Petegem [b], Bo Chen [f,*]

[a] Suzhou Laboratory, Suzhou 215123, China
[b] Structure and Mechanics of Advanced Materials, Center for Photon Science, Paul Scherrer Institute, Villigen 5232, Switzerland
[c] Center for Neutron and Muon Sciences, Paul Scherrer Institute, Villigen 5232, Switzerland
[d] Department of Industrial and Materials Science, Chalmers University of Technology, Gothenburg SE 412-96, Sweden
[e] Center for Nuclear Engineering and Sciences, Center for Photon Science, Paul Scherrer Institute, Villigen 5232, Switzerland
[f] School of Engineering, University of Southampton, Southampton SO17 1BJ, United Kingdom

ARTICLE INFO

Keywords:
Laser powder bed fusion
Synchrotron X-ray diffraction
Martensite
Phase transformation
Tool steel

ABSTRACT

A mechanistic understanding of phase transformation behaviour under extreme thermal conditions is essential for controlling microstructure and performance of additively manufactured metallic components. However, direct experimental evidence capturing phase evolution during rapid solidification remains limited. In this study, phase transformations in M50 tool steel processed by laser powder bed fusion (LPBF) were investigated using operando X-ray diffraction in reflection mode to monitor phase evolution during laser melting and subsequent cooling processes. Under cooling rates in the order of 10^5 °C/s, austenite formed directly from the liquid while δ-ferrite formation was suppressed. Martensitic transformation proceeded in a stepwise manner, with significant changes in phase fraction occurring at different cooling stages, highlighting the influence of rapid solidification on martensite nucleation and growth. Distinct transformation stages were identified, consisting of early abrupt transformation stages followed by later stages characterised by more gradual transformation. The carbon content in martensite increased from 0.58 ± 0.04 wt% to 0.68 ± 0.02 wt%, as determined from the evolution of local tetragonality. While variations in LPBF volume energy density had a limited effect on the cooling rate, lower energy densities were associated with higher martensite tetragonality and carbon enrichment. These findings provide valuable insights into phase evolution in rapid solidification processes for tailoring microstructure through manufacturing process control in additively manufactured steels.

1. Introduction

Laser powder bed fusion (LPBF), as a metal additive manufacturing (AM) technique, has been successfully applied to the fabrication of several tool steels, including H13 steel [1], M2 steel [2], CrMoV hot-work tool steel [3], and high-speed steels such as HS6–5–3–8 [4] and M3:2 [5]. M50 tool steel, the focus of this study, is widely used in aerospace, bearing, and tooling applications, due to its excellent high-temperature mechanical properties, attributed to its predominantly martensitic microstructure and fine precipitates. Previous studies have consistently shown that LPBF M50 steel exhibits good processability, refined microstructures and excellent mechanical properties. Saewe *et al.* [6] was the first to successfully process crack-free M50 steel by LPBF, achieving a high hardness of over 62 HRC (approximately 658 HV). Qin *et al.* [7] fabricated highly dense M50 steel using LPBF, achieving a relative density of above 99.9% and a high hardness of up to 850 HV. Kunz *et al.* [8] reported that M50 steel processed by LPBF exhibited a significantly smaller grain size (2.8–5.5 μm) compared to its conventionally manufactured counterpart (15.6–22.1 μm) produced by vacuum induction melting and vacuum arc remelting (VIM-VAR). This grain refinement contributed to a high hardness of 789 HV and a fatigue strength of 1180 MPa. This refinement also helps to minimise the presence of large primary carbides, which can otherwise compromise the mechanical properties of the steel, e.g. by initiating butterfly defects

* Corresponding authors.
E-mail addresses: zhanghy01@szlab.ac.cn (H. Zhang), b.chen@soton.ac.uk (B. Chen).

https://doi.org/10.1016/j.addma.2026.105323
Received 23 April 2026; Received in revised form 12 July 2026; Accepted 28 July 2026
Available online 29 July 2026

under rolling contact conditions [9]. Therefore, LPBF emerges as a promising manufacturing route for tool steels. However, the nature of the phase transformation behaviour and its underlying mechanisms during LPBF processing remain poorly understood.

The martensitic phase transformation plays a crucial role in determining the mechanical properties. A deeper understanding of martensitic formation kinetics, particularly during the LPBF process, could facilitate the development of advanced high-performance steels tailored for AM. Conversely, an incomplete understanding may lead to stress concentrations, potentially initiating cracks [10] or compromising the dimensional accuracy of the AM-built parts [11]. The martensite start temperature M_s is a key parameter that defines the onset of the austenite-to-martensite transformation. Donachie and Ansell [12,13] observed M_s increases with higher cooling rates. Specifically, they reported a 73 ℃ increase in M_s at a cooling rate of over 1.8×10^4 ℃/s compared to a lower rate of 8.0×10^3 ℃/s in a high carbon steel (0.76 wt% C). They attributed the M_s dependence to carbon diffusivity in austenite, where rapid cooling leads to an uneven carbon distribution, reducing austenite stability and thereby raising the M_s. In contrast, LPBF processed steels typically exhibited highly refined austenite grains and the increased grain boundary area can provide abundant nucleation sites for martensite [14]. Grain refinement also strengthened the austenite, impeding martensitic transformation and thereby reducing M_s [15].

Although many studies have investigated the effects of heat treatment conditions on martensitic transformation (e.g., [16,17]), the rapid cooling and thermal cycling inherent to the LPBF process, likely result in distinct martensite behaviour as revealed in the present study. A significant limitation of prior investigations into martensitic phase transformations arises from the inherent constraints associated with the experimental methodologies employed. Widely adopted *ex situ* characterisation methods, although valuable, provide only partial insights, namely, revealing the final microstructure state but failing to capture the dynamic processes. Therefore, efforts are needed to elucidate the martensitic transformation mechanisms specific to the LPBF process through *in situ* observations.

Operando X-ray techniques with high temporal resolution enable direct observation of non-equilibrium phase transformations under AM conditions [18]. For example, by tracking characteristic diffraction peaks, the phase transformation kinetics of β-Ti to α-Ti in Ti−6Al-4V during the rapid cooling of LPBF process have been extensively studied [19,20]. Glerum *et al.* [21] used this technique to capture rapid elemental reactions in pre-alloyed Al-Sc-Zr powder, occurring within 300 μs at high temperatures near the Al melting point during laser melting. For AM steels, Konig *et al.* [22] used operando X-ray diffraction to investigate the solidification mode of LPBF hot-work tool steel, focusing on the transition from primary δ-ferrite to primary γ solidification with increasing solidification velocity. Epp *et al.* [23,24] employed the technique to study evolution of phase transformations in X40CrMoV5–1 steel, focusing on the effects of intrinsic heat treatment during deposition. Gao *et al.* [25] further applied operando X-ray diffraction to 316 L stainless steel to probe dislocation density in solid phases and its dynamic evolution during solidification and subsequent cooling.

In this work, the phase evolution of LPBF M50 steel, including both liquid-to-solid and solid-to-solid transformations, was investigated, demonstrating the capability of the operando LPBF setup to track phase transformations in tool steel during processing. Temperature profiles under the rapid solidification and associated carbon redistribution were analysed. Notably, the stepwise martensitic transformation observed during rapid cooling represents, to the best of the authors' knowledge, is the first reported instance in AM steels. These findings provide crucial insights into phase evolution pathways during rapid solidification in AM, enabling improved process control and microstructural tailoring for enhanced mechanical performance of AM metals.

2. Methods

2.1. Operando X-ray diffraction

M50 tool steel powder feedstock was produced using vacuum induction melting and inert-gas atomisation, and its chemical composition determined by inductively coupled plasma analysis meets the ASTM standard specifications [26], Table 1. The powder was mostly spherical, with some satellite particles observed, as shown in Fig. 1a. The particle size distribution was determined by laser diffraction, yielding D_{10}, D_{50}, and D_{90} values of 19.27 μm, 33.65 μm, and 57.63 μm, respectively, with the corresponding size distribution plot presented in the inset. Overall, the M50 powder exhibits characteristics suitable for LPBF fabrication.

Operando X-ray diffraction experiments were conducted using a miniaturised LPBF printer at the microXAS beamline of Swiss Light Source, Switzerland. Fig. 1b schematically depicts the experimental setup. Steel powder was spread on the baseplate, with the X-Y plane representing the top view and the Z-axis for the AM-build direction. The monochromatic X-ray beam with an energy of 17.18 keV was focused to a spot size of 54 μm × 27 μm (horizontal × vertical) and directed onto the sample. The printer was tilted by 15° towards the incident X-ray beam, resulting in a projected area of 104 μm × 54 μm. The X-ray beam was positioned 2 mm from the outer edge of the build plate near the detector. Two-dimensional (2D) diffraction patterns were recorded with an EIGER 1 M detector in reflection mode at an acquisition rate of 20 kHz (exposure time: 0.05 ms). These 2D images were reduced to conventional one-dimensional (1D) diffraction spectra by azimuthal integration using pyFAI [27]. Matlab scripts developed in-house were applied to track the positions and intensities of diffraction peaks. More details on the MiniSLM setup can be found elsewhere [19,28].

During the sample printing process, laser beam with a diameter of 45 μm was used, along with a powder layer thickness of 0.03 mm. The printer chamber was continuously flushed with high-purity Ar gas. The LPBF parameter sets are summarised in Table 2. They were selected to ensure good steel processability and sufficient melt pool stability, minimising powder spattering for reliable diffraction data collection. The volume energy density was calculated using the equation $E_v = P/(vdh)$, in which P is the power, v is the scanning speed, h is the hatch distance, and d is the layer thickness.

After printing, the samples were ground and polished to a final finish using 1 μm diamond suspensions. Chemical etching was then performed using 2% nital solution. Micrographs of the as-printed M50 steel were taken in back-scattered electron (BSE) mode of scanning electron microscopy (SEM) on an FEI Quanta 650 FEG-SEM. Electron back-scatter diffraction (EBSD) samples were prepared by vibratory polishing and characterised using a TESCAN MIRA FEG-SEM. The micro-hardness was measured using a QNESS Q10 CHD automatic tester equipped with a Vickers indenter under a load of 300 g and a dwell time of 15 s.

2.2. Data analysis

To visualise the phase transformation sequence during the LPBF process, the integrated diffraction patterns were organised into an intensity map. Fig. 2a shows the phase evolution before, during, and after laser manufacturing of the top layer of Sample 1 with time on the vertical axis and diffraction angle (2θ) on the horizontal axis. Intensity (counts per pixel) is colour-mapped, where the baseline appears in dark blue, and peaks rising above the baseline are shown in green/yellow. The inset, marked by a red dashed box, shows an enlarged view of the γ(200) peak evolution as the steel powder within the X-ray interaction volume experienced cyclic heating and cooling during laser scanning. Intensity maps of other samples are provided in Appendix A.

The corresponding temperature profiles were estimated by tracking the γ(311) diffraction peak that is insensitive to texture evolution [29], allowing to derive the lattice strain from which the macroscopic strain can be estimated [30]. By linking this with the coefficient of thermal

Table 1
Chemical composition (wt%) of M50 steel powder in comparison to the ASTM standard specification.

Element	C	Mo	Cr	V	Si	Mn
Powder	0.79	4.19	4.36	1.15	0.42	0.34
ASTM	0.78–0.88	3.90–4.75	3.75–4.50	0.80–1.25	0.20–0.60	0.15–0.45

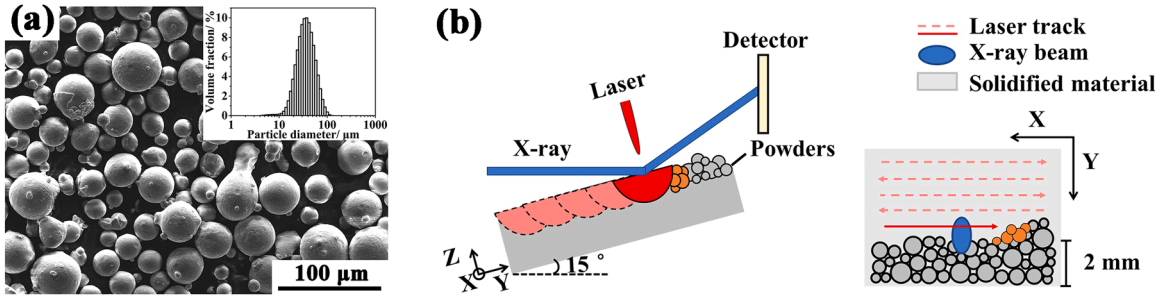

Fig. 1. (a) SEM micrograph of M50 steel powder, with particle size distribution shown in the inset; (b) schematic of the experimental setup in reflection mode for operando X-ray diffraction.

Table 2
LPBF process parameters of samples for operando X-ray diffraction experiments. E_v: Volume energy density.

Sample ID	Power/ W	Speed/ mm•s^{-1}	Hatch distance/ mm	E_v/ J•mm^{-3}
1	150	800	0.05	125.00
2	125	800	0.05	104.17
3	150	500	0.05	200.00
4	125	500	0.03	277.78

expansion (CTE), a consistent temperature estimation can be attained.

Fig. 2b presents the lattice parameter a for the γ(311) peak during the repeated melting and solidification cycles, which was calculated using the following equation:

$$a = \frac{\lambda}{2\sin\theta}\cdot\sqrt{h^2+k^2+l^2} \quad (1)$$

where λ is the wavelength with a value of 0.72 Å, θ is half of the diffraction angle, and h, k, l are the Miller indices. It is assumed that the peak shift during heating and cooling is primarily due to isotropic thermal expansion and contraction, without considering the effect of

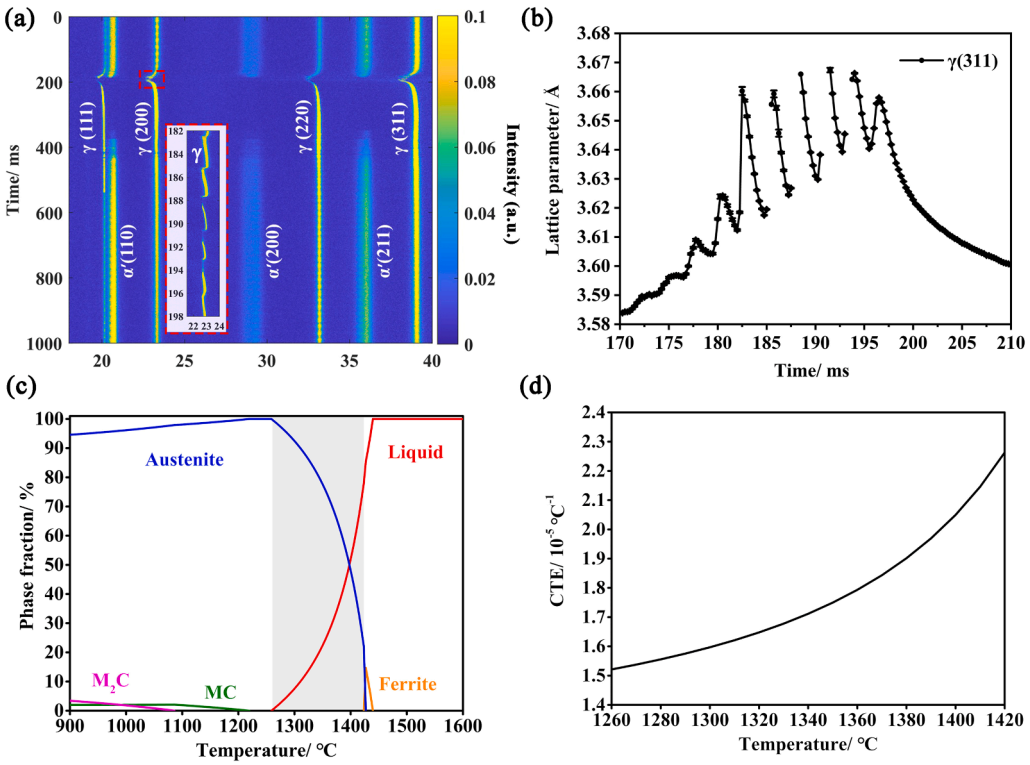

Fig. 2. (a) Evolution of diffraction patterns as a function of time measured by the X-ray beam on the surface layer during laser scanning (Sample 1, laser power: 150 W; scanning speed: 800 mm/s; hatch distance: 0.05 mm). The inset highlights oscillations of peak positions under repeated heating and cooling cycles. (b) lattice parameter evolution of γ(311) peak during melting and solidification cycles. The error bars for some data points are covered by the markers due to the smaller magnitudes. (c) CALPHAD-based phase fraction predictions during equilibrium solidification and (d) CTE calculated by JMatPro.

residual stresses or compositional changes.

The lattice strain at any time t was derived using the relation of $\varepsilon_t = -\cot\theta_t \cdot (\theta_t - \theta_0)$, where θ_t is the half-diffraction angle of the peak at t. θ_0 is the reference half-diffraction angle at $t = 0$ ms, corresponding to the initial measurement of the powder at ambient temperature (25 ℃). The temperature was then estimated from the lattice strain for the liquid-to-solid transformation process, using the equation $\varepsilon_t = C \cdot \Delta T$ with the known C (coefficient of thermal expansion, CTE). ΔT is the temperature difference relative to the ambient temperature. A similar approach was adopted in a previous study [31]. The CTE values were determined through thermodynamic calculations using JMatPro (version 12.4; database: General Steel) [32]. The phase prediction for M50 steel under the equilibrium solidification condition indicates the liquidus temperature of 1440 ℃, with solidification completing at 1260 ℃, as shown in the shaded region of Fig. 2c. The CTE values within the temperature range of 1260–1420 ℃, where only liquid and austenite phases are thermodynamically predicted to exist in the M50 steel system, are presented in Fig. 2d. For simplicity, a constant CTE value of 2.25×10^{-5} $℃^{-1}$, corresponding to the temperature at 1420 ℃ when the liquid phase is predicted to start transforming into austenite, was selected for the qualitative evaluation of temperature profiles.

The assessment of phase evolution was based on the principle that the total intensity of all diffraction peaks for a given phase is proportional to its volume fraction [33]. As shown in Fig. 2a, the diffraction peaks tracked during solidification include γ{111}, γ{200}, γ{220}, and γ{311} for austenite; while α′{110}, α′{200}, and α′{211} for martensite.

Taking austenite γ as an example, for a given diffraction peak i of austenite, its intensity can be expressed as [33]:

$$I_\gamma = \frac{KR_\gamma c_\gamma}{2\mu} \tag{2}$$

where

$$R_\gamma = \left(\frac{1}{V^2}\right)\left[|F|^2 p\left(\frac{1+\cos^2 2\theta}{\sin^2\theta\cos\theta}\right)\right](e^{-2M}) \tag{3}$$

In Eq. (2), K is a constant, independent of the diffraction substance; μ is the linear absorption coefficient; c_γ is the volume fraction of γ-phase and R_γ is a scalar. Eq. (3) provides the mathematical description of R_γ. V is the unit cell volume which is derived from the lattice parameter; F is the structure factor; p is the multiplicity factor which depends on the crystal structure; and e^{-2M} is the temperature factor.

Similarly, the intensity of martensite α′ is given by:

$$I_{\alpha'} = \frac{KR_{\alpha'} c_{\alpha'}}{2\mu} \tag{4}$$

Thus, the volume-fraction ratio of $c_\gamma/c_{\alpha'}$ can be obtained by taking the intensity ratio of I_γ to $I_{\alpha'}$, yielding:

$$\frac{c_\gamma}{c_{\alpha'}} = \frac{I_\gamma R_{\alpha'}}{I_{\alpha'} R_\gamma} \tag{5}$$

The austenite volume fraction c_γ in a γ + α′ two-phase system can be estimated from the relation:

$$c_\gamma = \frac{\frac{1}{n}\Sigma_{i=1}^{n}\frac{I_{\gamma i}}{R_{\gamma i}}}{\frac{1}{n}\Sigma_{i=1}^{n}\frac{I_{\gamma i}}{R_{\gamma i}} + \frac{1}{m}\Sigma_{i=1}^{m}\frac{I_{\alpha' i}}{R_{\alpha' i}}} \tag{6}$$

where n and m represent the number of peaks used for phase determination of austenite ($n = 4$) and martensite (m=3), respectively.

3. Results

3.1. Solidification and thermal condition

Fig. 3 shows the time-resolved evolution of diffraction patterns captured from the top layer by the X-ray beam. As the laser beam approached the X-ray beam probed region, the powder underwent rapid heating, resulting in a peak shift to lower diffraction angles due to thermal expansion and gradually recovered due to cooling as the laser moved away. When the laser beam came even closer, the powder reached elevated temperatures, causing the disappearance of α′-phase peaks at about 185 ms. Meanwhile, γ-phase peaks experienced cyclic shifting back and forth, indicating the repeated thermal fluctuations induced by the snake-like scanning strategy.

The inset in Fig. 3 (highlighted by a red box) provides a magnified view of the rapid melting and solidification processes. When the laser entered the probed region, all diffraction peaks vanished momentarily, indicating complete melting within the probed volume. As the laser beam moved away, γ-phase diffraction peaks appeared first. However, the thermodynamic calculations (Fig. 2c) predict δ-ferrite as the first stable phase to form during equilibrium solidification. The absence of δ-ferrite in the experimental data suggests that its formation was probably suppressed. Due to the extremely short lifetime of transient diffraction peaks during rapid solidification, it is also possible that δ-ferrite existed only briefly and was not experimentally captured.

Fig. 4a presents the estimation of temperature based on the lattice parameter evolution of γ(311) peak. Temperature is shown only when austenite diffraction peaks are detectable. The evolution of the γ phase was monitored following melting, during which the maximum calculated temperature reached 1290 °C. This is consistent with the liquid-austenite transformation temperature range (1260 ℃ to 1440 ℃) in the thermodynamic calculations, Fig. 2c. The temperature profile was fitted by an exponential decay function: $T = T_0 + Ae^{-(t-t_0)/\tau}$, where T_0 and t_0 are the temperature and time when the incipient solid was detected at the start of cooling. A is the initial amplitude and τ is the decay constant. Two tracks overlaid in a red curve in Fig. 4a represent the fitting results of the temperature function during the solidification process.

The cooling rate dT/dt of the solidification process was derived from the first derivative of the fitted temperature function. Fig. 4b presents the calculated cooling rate from two tracks where materials solidified after fully melting. The cooling rate observed was in the order of 10^5 ℃/s which agrees reasonably well with the reported cooling rate of rapid solidification for laser printing [22,34]. The initial cooling rates of the two tracks were comparable, both reaching approximately 6×10^5 ℃/s at the highest temperature of 1290 ℃. However, discrepancies became more pronounced as cooling continued over time. Track 2, which followed Track 1, exhibited a lower cooling rate. This difference arises from the sequential laser line-scanning strategy, where the material in the probed region underwent initial solidification during Track 1 before being remelted and resolidified in Track 2. The surrounding temperature during the solidification of Track 2 was higher than that of Track 1, resulting in a reduced temperature gradient and consequently a lower cooling rate [35]. In this study, the track with the highest cooling rate, corresponding to the first instance of full melting in the probed region, was used for the cooling rate determination across all samples, to ensure consistency in the extracted thermal profiles.

Fig. 4c presents the cooling rates determined for all samples from the laser track in which the probed region was first melted. Overall, the cooling rates are in the order of 10^5 ℃/s for all processing conditions. Sample 1, processed at a volume energy density of 125 J•mm^{-3}, exhibited the highest cooling rate among all samples, while Sample 4 processed at the highest volume energy density of 277.7 J•mm^{-3}, had the lowest initial cooling rate of 3.7×10^5 ℃/s and the slowest decay during the first 1 ms of cooling. Fig. 4d presents the average cooling rate over the initial 1 ms as a function of volume energy density. The cooling rate varied around 3×10^5 ℃/s across all samples. At relatively low energy densities, the average cooling rate decreases to a minimum of 2.1×10^5 ℃/s at E_v= 104.17 J•mm^{-3}, followed by an increase to a maximum of 3.8×10^5 ℃/s at E_v= 125 J•mm^{-3} and then a gradual decrease at higher energy densities. The results indicate that the cooling

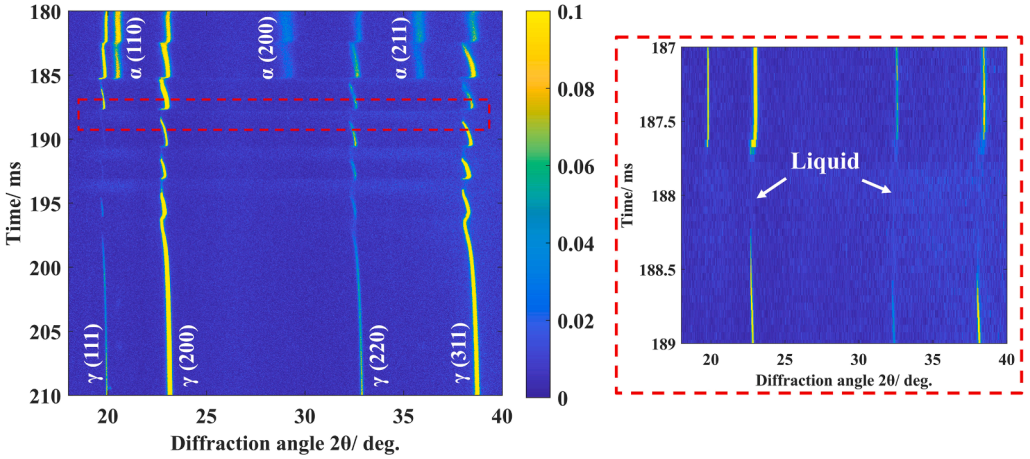

Fig. 3. Evolution of diffraction patterns collected from Sample 1, with the enlarged view showing that the γ-phase is the first solid phase during the liquid cooling.

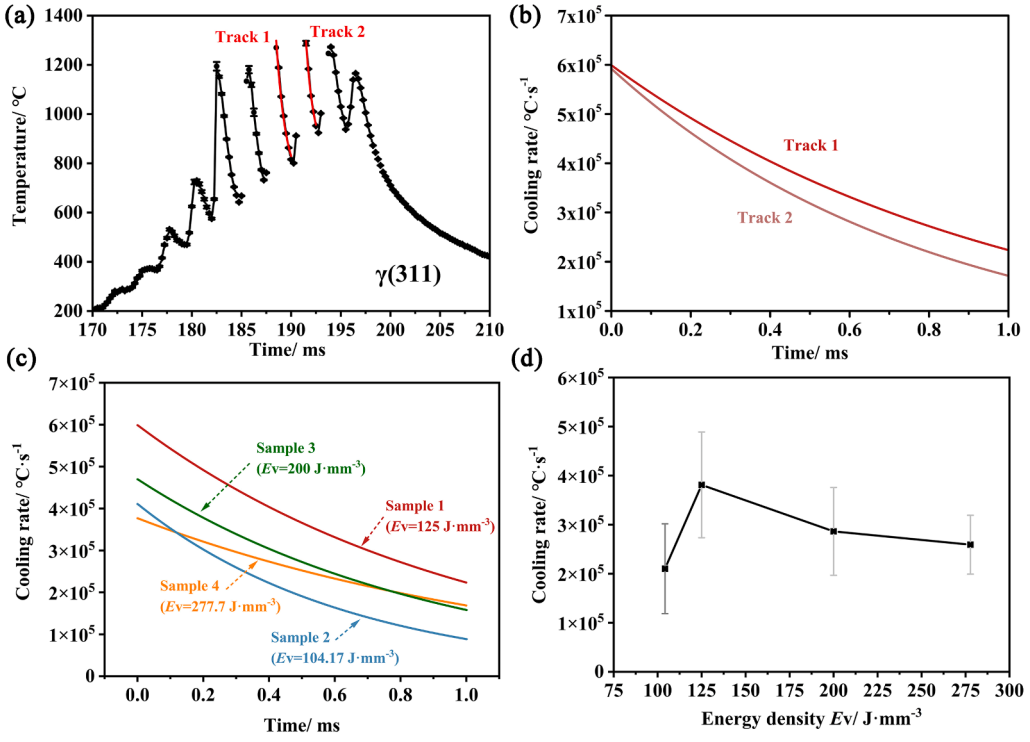

Fig. 4. (a) Calculated temperature profile based on the lattice expansion/contraction of γ(311); (b) cooling rate obtained from the first derivative of fitted temperature from the individual tracks in (a); (c) cooling rates of all samples as a function of time, labelled in different colours; (d) average cooling rate within 1 ms of all samples, as a function of volume energy density.

rate in LPBF steel is not governed by energy density only. It could reflect the combined effects of energy input, melt pool geometry and local heat transfer conditions which warrant further investigation.

3.2. γ-α′ transformation in LPBF process

Martensite phase was observed upon continued cooling, revealing the transformation from the austenite to martensite. Fig. 5a presents a series of diffraction patterns of Sample 1 at different time points where diffraction peaks corresponding to both austenite and martensite phases were identified. Initially, the diffraction patterns predominantly exhibited the γ phase, such as the strong γ(220) and γ(311). The intensity of the α′ reflections increased progressively with time, accompanied by a corresponding reduction in γ phase intensity, as evidenced by the evolution of the γ(311) and α′(110) peaks. This indicates the progressive transformation from γ to α′. Fig. 5b presents the quantified evolution of austenite and martensite phase fractions as a function of time during cooling. The martensite first became detectable at approximately 365 ms, at which point the austenite fraction began to decrease from an initial value of 0.97 ± 0.007. As the transformation progressed, a substantial increase in martensite formation was observed, leading to a reduction in austenite content. The three distinct step-like increases in martensite fraction, as exhibited in the figure, at around 373 ms, 430 ms and 530 ms, suggest that the martensitic transformation proceeded in rapid bursts rather than as a continuous process.

Fig. 5c presents an enlarged view of the martensite phase fraction, revealing the detailed burst-like feature of the phase transformation. The diffraction patterns in the upper panel display a magnified region of

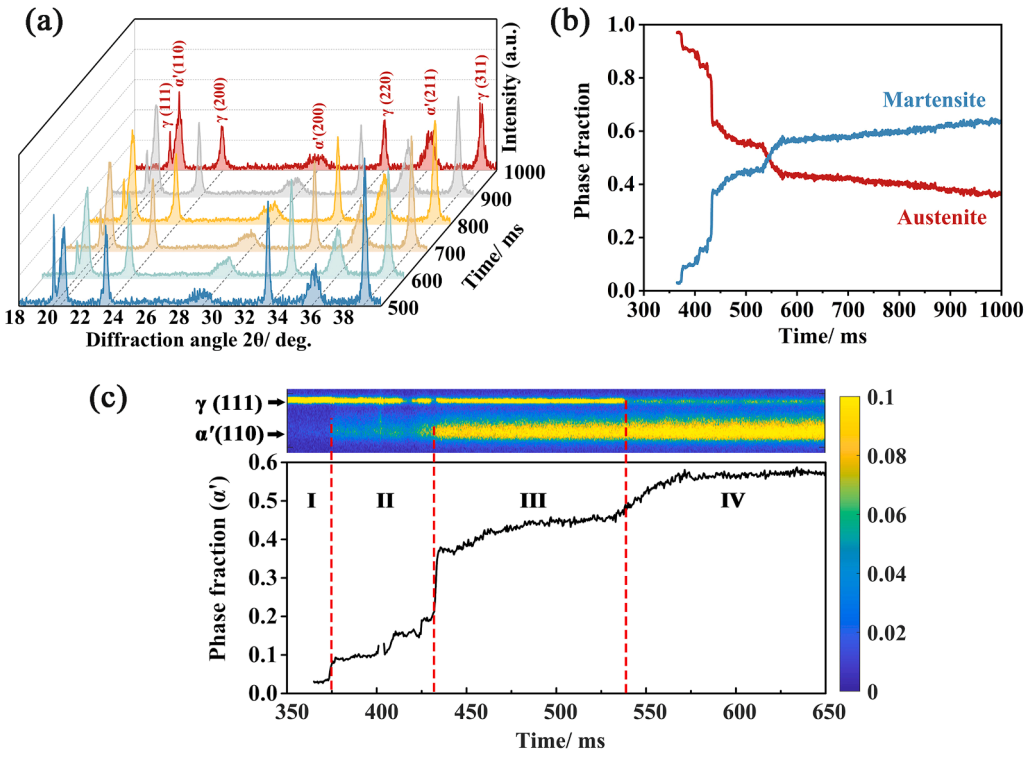

Fig. 5. (a) Representative diffraction patterns collected during the cooling process of Sample 1, showing the evolution of austenite and martensite peaks; (b) phase fraction evolution of austenite and martensite as a function of time; (c) martensite phase fraction as a function of time with α′(110) and γ(111) diffraction peaks shown in the upper panel, highlighting the stepwise martensitic transformation.

the full intensity map (Fig. 2a) over the corresponding time interval, showing the evolution of the α′(110) and γ(111) peaks as direct indicators of changes in diffraction intensity. Both the martensite fraction and diffraction intensity exhibited significant increases during cooling, highlighting a stepwise transformation process that can be categorised into four distinct stages, as delineated by the red dashed lines:

- Stage I (365–373 ms): the initial martensitic transformation occurred once the temperature dropped below M_s, with an abrupt phase fraction increase to 0.03;
- Stage II (373–430 ms): a rapid increase in martensite fraction by 0.05 was observed, followed by a gradual increase to 0.19;
- Stage III (430–532 ms): martensite formation proceeded with an initial increase of 0.18, followed by a more gradual rise from 0.37 ± 0.001–0.46 ± 0.001;
- Stage IV (> 532 ms): the phase fraction of martensite continued to increase moderately, reaching 0.56 ± 0.0002 at 570 ms, after which it increased much more slowly.

This stepwise transformation behaviour has been consistently observed across all samples studied in the present work (Appendix A). The underlying mechanisms driving these discrete transformation stages as well as the martensitic transformation kinetics will be discussed later in Sections 4.2 and 4.3. In Stage II, minor fluctuations in the phase fraction occurred at around 404 ms and 424 ms. These variations are likely attributed to low peak intensities collected by the detector. The temporary reduction in diffraction intensity was likely caused by a partial obstruction of the diffracted X-ray beam due to spatters generated during the manufacturing process in the chamber.

3.3. Martensite tetragonality

A key contribution to the outstanding hardness of high-carbon steels stems from the carbon atoms interstitially occupying one of the octahedral sites within the martensite lattice, inducing a body-centred tetragonal (BCT) distortion that enhances its strength and rigidity [36]. The martensite tetragonality, evaluated by the ratio of lattice parameters c and a, is a crucial factor influencing the material properties. To this end, diffraction patterns collected after LPBF printing were systematically analysed, focusing on the characteristic martensite peaks to elucidate the evolution of lattice distortions.

Fig. 6a1 presents the diffraction pattern of Sample 1 collected after printing. The martensite phase fraction was quantified as 0.69 ± 0.001, which agrees well with the operando X-ray diffraction analysis, yielding a martensite phase fraction of 0.64 ± 0.001 at t = 1000 ms (Fig. 5b). This agreement supports the reliability of the operando measurement. The high content of retained austenite is one of the characteristics of AM steel due to the rapid solidification and high cooling rate, resulting in the low diffusion rate of carbon and alloy atoms remaining in the austenite phase [37]. The martensite tetragonality was evident in the broad {200} diffraction peak, highlighted within the red box in Fig. 6a1. Due to the presence of interstitial carbon atoms in the lattice, the {200} peak splits into two peaks. Fig. 6a2 shows an enlarged view of the {200} peak where peak fitting using the Pearson VII function successfully separated the overlapped (200) and (002) reflections, represented by dashed curves in different colours. The residuals between the fitted model and experimental data, as displayed in the bottom sub-figure, were in the range of ±0.005, indicating a high-quality peak fitting and reliable peak determination. The martensite tetragonality represented by the c/a ratio, was calculated as 1.020 ± 0.0002 based on the lattice parameters of c = 2.897 ± 0.0005 Å and a = 2.840 ± 0.0004 Å derived from the separated peak positions. The martensite tetragonality has been reported to vary linearly with the carbon content, following the relationship of the equation of c/a= 1 + 0.031 ×C (wt%), which has been confirmed for steels with various carbon concentrations [38,39]. Given the nominal carbon content of ~0.8 wt% in M50 tool steel, the expected c/a ratio is approximately 1.025, which is slightly higher than the experimentally measured value.

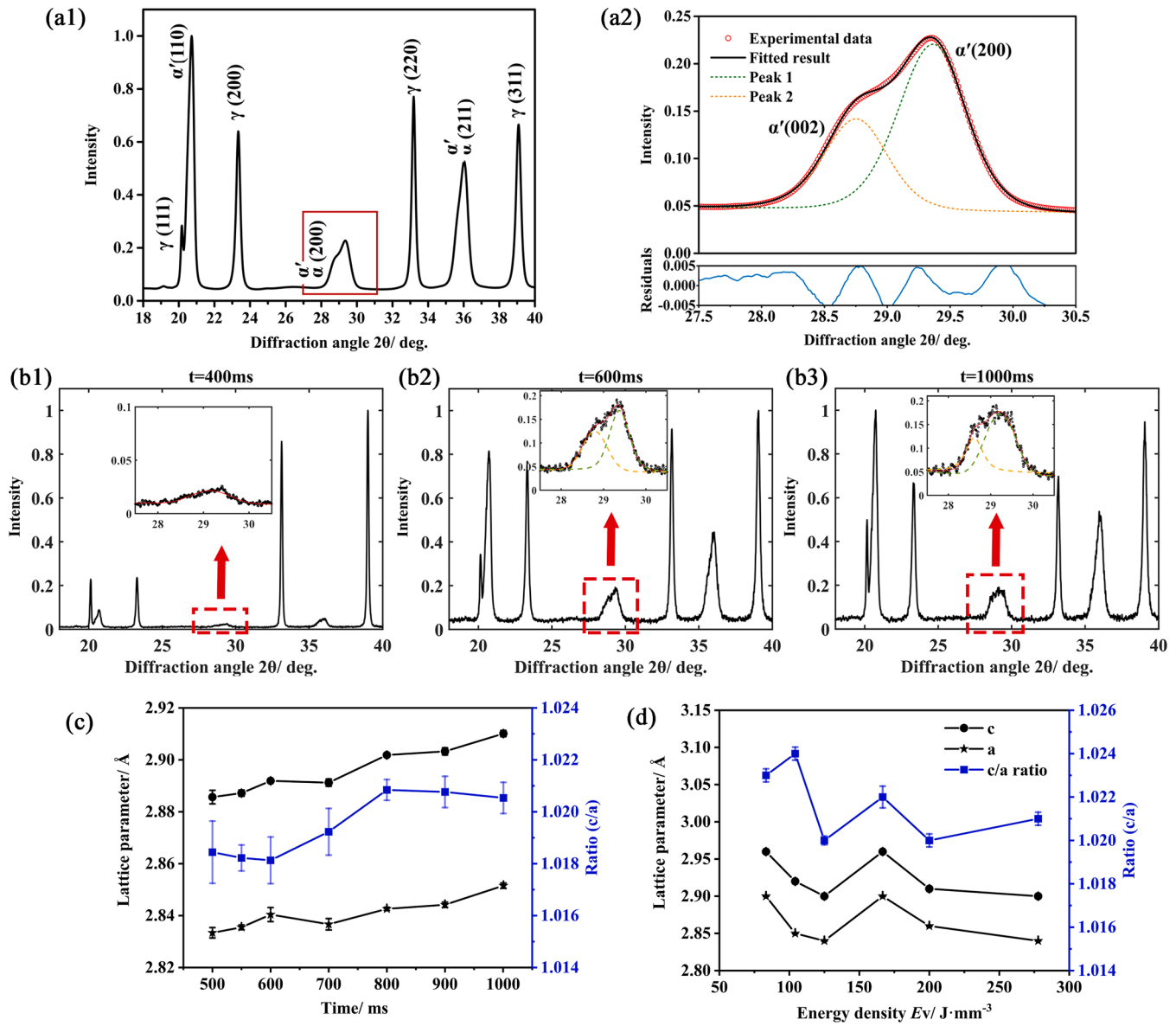

Fig. 6. (a1) Normalised diffraction pattern collected after laser printing of Sample 1, showing the diffraction peaks of α′-Fe (martensite) and γ-Fe (austenite). The characteristic martensite α′(200) peak was marked in a red box; (a2) enlarged view of the marked peak in (a1), showing the fitting results and the residuals; (b1-b3) normalised diffraction patterns collected at 400 ms, 600 ms, and 1000 ms, respectively, showing the progressive peak splitting; (c) evolution of the martensite lattice parameters (*c* and *a*) extracted from the α′(200) peak, along with the calculated *c*/*a* ratio as a function of time during the cooling process; (d) lattice parameters and corresponding *c*/*a* ratio of martensite for all samples, plotted as a function of volume energy density. For some data points, the error bars are barely visible because their magnitudes are smaller than the marker size.

Fig. 6b1 to b3 present the diffraction patterns collected during the transformation process at 400, 600, and 1000 ms, respectively, showing the progressive peak splitting of the {200} reflection. Martensite peaks first become identifiable at around 365 ms (Fig. 5c). Therefore, they are observed at 400 ms, although their intensity remains relatively weak and the {200} reflection appears as a single peak. As the transformation proceeds, martensite tetragonality becomes evident through the broadening and splitting of the {200} reflection into two components.

Fig. 6c presents the evolution of the determined lattice parameters (*c* and *a*) and their ratio (*c*/*a*) during the cooling process. Note that the tetragonal distortion of martensite only became measurable after approximately 500 ms, when the {200} peak intensity appeared sufficiently strong to resolve the distinct (200) and (002) reflections. Previous studies have commented on critical carbon thresholds for the formation of tetragonal martensite. Liu *et al.* [40] theoretically estimated that martensite in steel exhibited tetragonality when its carbon content exceeded 0.18 wt%, while the tetragonal splitting of diffraction peaks occurred at the carbon content above 0.55 wt%. Sherby *et al.* [41] reported that martensite had a cubic structure at a carbon content below 0.6 wt% C but transformed to a tetragonal structure beyond this threshold [42,43]. Similarly, Tanaka *et al.* [44] observed that tetragonal martensite started to appear when the carbon content was over 0.44 wt %. In the present study, the tetragonal splitting of the martensite peaks was first detected at a *c*/*a* ratio of 1.018 ± 0.0012 (blue curve in Fig. 6c), corresponding to an estimated carbon content of 0.58 ± 0.04 wt%, which aligns well with previously reported values. As the transformation progressed, the lattice parameters exhibited a gradual increase, with *a*-value increasing from 2.833 ± 0.0020 Å to 2.852 ± 0.0010 Å and *c*-value increasing from 2.886 ± 0.0026 to 2.910 ± 0.0012 Å (black curves in Fig. 6c). Consequently, the *c*/*a* ratio increased from 1.018 ± 0.0012 to 1.021 ± 0.0006, indicating an increase in the estimated carbon content from 0.58 ± 0.04 wt% to 0.68 ± 0.02 wt% in the

martensite phase. This increase is likely associated with the progressive enrichment of carbon in the austenitic parent phase during transformation. The uncertainties in the c/a ratios were estimated by propagating the fitting errors of the lattice parameters c and a. The corresponding uncertainty was also propagated into the carbon content calculated using the empirical relationship between martensite tetragonality and carbon content.

It is noted that the estimation of carbon content was based on the calculation of lattice parameters, which should be regarded as semi-quantitative rather than an independent compositional measurement. LPBF-induced residual stresses can influence the lattice parameter through elastic strain. However, they are unlikely to account for the lattice parameter evolution observed here. As shown in Fig. 6c, the lattice parameter increased from 2.88 to 2.90 Å between 500 and 1000 ms. Using the conventional definition of lattice strain, this corresponds to a strain of approximately 7000 με. Assuming a typical Young's modulus of 200 GPa for steel, this would imply an equivalent elastic stress of ~1400 MPa, which is unrealistically high for LPBF-induced residual stresses. Furthermore, after martensite formation begins (below 300 ℃), most processing-induced residual stress fields would already have been established while the subsequent cooling stage involves lower thermal gradients and limited additional stress accumulation. Therefore, the lattice parameter evolution measured by operando X-ray diffraction cannot be attributed solely to residual stress but likely also reflects mechanisms associated with martensitic transformation.

The effect of manufacturing parameters on martensite tetragonality was further investigated by comparing the c/a ratios of different samples. Fig. 6d presents the lattice parameters and c/a ratio as determined from all samples after printing. There is no clear linear correlation between tetragonality and volume energy density. With increasing energy density, the lattice parameters varied within a narrow range of 0.02 Å (a: 2.84–2.86 Å; c: 2.90–2.92 Å), while the c/a ratio varied between 1.020 and 1.024, slightly lower than the theoretical value of 1.025 for 0.8 wt% C steel. The sample fabricated at the lowest energy density exhibited the smallest deviations from the expected martensite tetragonality, suggesting that energy input may influence the degree of lattice distortion.

3.4. *Ex situ characterisation*

Fig. 7a presents the top layer microstructure of as-printed LPBF M50 steel (Sample 1). The layer-by-layer nature of LPBF M50 steel microstructure is clearly visible along the build direction, as indicated by the black arrow. A distinct contrast is observed between the topmost layer and the underlying layers, potentially arising from the repeated heating cycles where the previously deposited material was tempered. In contrast to the subsurface layers, the top layer does not experience additional heat treatment from subsequent passes and is therefore subjected to a lower degree of tempering. Similar microstructural contrasts between the top layer and subsurface layers have also been reported in other LPBF alloys [34,45]. An enlarged view of the microstructure is provided in the inset at the lower right, showing the presence of both equiaxed and columnar grains that are the typical features of additively manufactured steels.

Fig. 7b presents the phase distribution map of the top layer obtained by EBSD. Martensite phase, shown in red colour, is the dominant phase with a determined fraction of 74.6%. The EBSD-derived phase fraction is slightly higher than the martensite fraction of 69% measured by *ex situ* X-ray diffraction (Fig. 6) which may be attributed to the difficulty of reliably indexing highly strained intercellular regions, together with differences in sampling volumes and quantification principles between the two techniques. Retained austenite was observed primarily at the intercellular regions of the LPBF steel, consistent with previous reports on retained austenite formation in AM steels [3]. The narrow intercellular channels were not indexed by EBSD, most likely due to the high residual stresses and dislocation densities localised in these regions, which distort the crystal lattice and hinder reliable Kikuchi pattern indexing. It is therefore reasonable to assume that these unindexed regions also contain retained austenite, leading to a slight overestimation of the martensite fraction by EBSD. The inverse pole figure (IPF) of martensite in the top layer (Fig. 7c) shows randomly oriented grains. The average grain diameter of 0.48 μm was derived from the corresponding grain size distribution diagram in Fig. 7d.

Fig. 7e shows the microhardness measurements of the top layer, obtained at five randomly selected locations at comparable distances from the sample surface. The hardness values exhibit minor variations, indicating a relatively homogeneous microstructure within the layer.

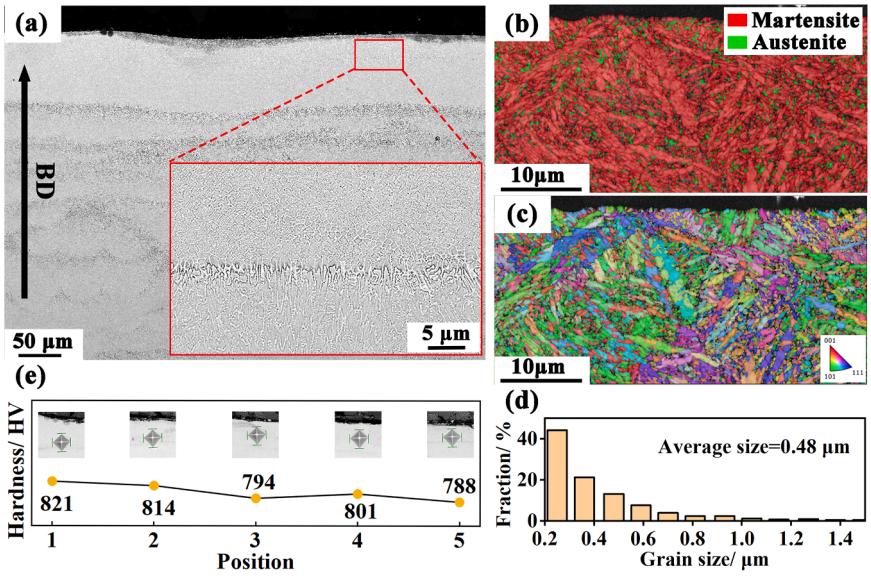

Fig. 7. (a) Microstructure of the top layer in LPBF M50 steel (Sample 1), with the build direction (BD) indicated by the black arrow; (b) EBSD phase map of the top layer showing the distribution of martensite (red) and austenite (green), with unindexed pixels displayed in dark contrast. The overall indexing rate was 0.72 without applying any data post-processing; (c) inverse pole figure (IPF) of martensite obtained from a cross-section parallel to the build direction; (d) grain size distribution of the top layer derived from EBSD analysis; (e) microhardness profiles measured at multiple locations within the top layer.

The average hardness of LPBF M50 steel in the as-built condition was determined to be 804 ± 14 HV, comparable to previously reported values for LPBF M50 steel [7]. Importantly, this is much higher than that of conventionally produced M50 steel via VIM-VAR, which exhibits a hardness of 681 HV (equivalent to 63 HRC [9]) after appropriate heat treatment, with secondary carbides distributed throughout the microstructure. The excellent mechanical performance of LPBF M50 steel can be attributed to its refined grain structure, a direct consequence of the rapid solidification inherent to the LPBF process. These findings highlight the promise of AM technique for future steel production and the critical importance of understanding phase transformation pathways under AM conditions to establish comprehensive processing-microstructure-property relationships in tool steels.

4. Discussion

4.1. Phase suppression during rapid solidification

The microstructures developed during the solidification of steels are influenced by alloy compositions and thermal conditions [46]. In this study, by employing the operando X-ray diffraction technique at LPBF conditions, the γ-Fe phase was observed as the only phase directly formed from the liquid phase in M50 tool steel under rapid solidification conditions at a cooling rate of 10^5 ℃/s. This contrasts with the thermodynamic predictions, where the δ-ferrite is expected to be the first solid phase, as shown in Fig. 2c. Similar findings were reported by Konig *et al.* [22], who observed that δ-ferrite was suppressed in AM hot work steel at a cooling rate of 10^6 ℃/s but was detected at a lower cooling rate of 10^4 ℃/s. This highlights the important role of thermal conditions on phase transformation paths. Moreover, rapid solidification accompanied by a high thermal gradient results in the development of a dendritic microstructure [47,48]. This microstructural feature has been commonly observed across various AM steels, including tool [5,49–51], stainless [52,53], transformation-induced plasticity (TRIP) [54], and maraging steel [55]. Chou *et al.* [3] calculated the dendrite tip temperature of steel matrix phases as a function of solidification velocity. They found that austenite (γ-Fe) exhibited a higher dendrite tip temperature than δ-ferrite at higher solidification velocities. This suggests that rapid cooling conditions promote the direct formation of γ-Fe, providing a plausible explanation for the absence of δ-ferrite in the present work (Fig. 3).

MC and M_2C carbides are predicted to precipitate alongside austenite during solidification, following equilibrium thermodynamic calculations (Fig. 2c). These primary carbides have been reported in M50 steel produced by casting [56] and hot-rolling [57,58]. However, owing to the high cooling rates, our observations indicate that only γ-Fe and α′-Fe were detected in M50 steel after rapid solidification. Although it remains possible that a minor fraction of carbides formed in subsequent solidification layers, their volume fraction was below the detection limit of operando X-ray diffraction.

The synchrotron X-ray diffraction measurements were made under reflection mode, meaning diffraction signals were collected only from the top layers (< 60 μm depth) instead of the underlying layers, which experienced thermal ageing due to heat conduction from the top. This ageing could potentially facilitate carbide formation [23]. Nevertheless, in larger M50 steel bulk samples produced by LPBF, no carbide was observed in the as-manufactured condition [6], and only a few fine carbides were visible after tempering heat treatments [8]. This suggests that the rapid solidification conditions in laser-based AM restricted carbide formation, in contrast to the slower cooling conditions of conventional means.

However, it is important to recognise the uncertainties in the cooling rate determination based on evolved peak positions. First, the cooling rate of 10^5 ℃/s was derived from the solid phase of γ-Fe in the probed region once its phase fraction reached a detectable level of X-ray diffraction (0.2 wt% for synchrotron X-ray [59]), neglecting the initial stage of liquid solidification. Therefore, the peak cooling rate of AM solidification processing is expected to be higher. Second, the probed region with a length of 104 μm was larger than the hatch distance of 50 μm, encompassing multiple laser tracks. As a result, the collected diffraction signals represented an average response of the material within the probed region rather than directly capturing the solidification front only.

Third, only thermal effects on lattice parameters were considered in the analysis, leaving out the residual stress, strain or potential compositional variations. Residual stresses in AM materials arise from the rapid heating and cooling, typically manifesting as tensile stresses near the top surface due to constrained contraction during solidification. For reference, Ahmad *et al.* [60] reported maximum tensile residual stress of 837 MPa in LPBF Inconel 718 and 920 MPa in LPBF Ti−6Al-4V. It should be noted that the cooling rate determined in this study corresponds to the early stage of solidification at elevated temperature where the residual stress level is expected to be lower than the values reported for components determined after manufacturing. Additionally, while the CTE is inherently temperature-dependent, it was approximated as a constant value for cooling rate estimation. The constant CTE value selected at a relatively high temperature (1420 ℃) in this study may lead to an underestimation of the absolute temperature values. However, the temperature profile was derived for cooling rate calculation, depending on the first derivative of the temperature curve rather than the exact temperature values. Glerum *et al.* [21] reported that using a constant CTE resulted in a ~5% misestimation of the temperatures experienced by the melt pool while the temperature profile exhibited almost the same trend as that obtained using a temperature-dependent CTE. Therefore, this simplification is not expected to affect the determined cooling rate results. To assess this effect, a sensitivity analysis was performed, with the results presented in Appendix B.

4.2. Thermodynamics of martensite formation

The nucleation of martensite is primarily driven by an energy change resulting from undercooling. The driving force consists of two components: (i) a chemical contribution expressed by the Gibbs free energy difference between the parent austenite and the martensite; (ii) energy barriers that oppose the transformation, including the elastic strain energy and the interfacial energy [61]. The elastic strain energy arises from the volumetric deformation associated with the martensite formation, while the interfacial energy corresponds to the energetic cost of generating the austenite/martensite boundary. Given the semi-coherent nature of the martensite-austenite interface, the interfacial energy contribution is minimal, making the elastic energy component the dominant non-chemical barrier to transformation.

Martensitic transformation is inherently accompanied by a volumetric deformation, generating elastic strain energy ΔG_{el}. This can be expressed as [62]:

$$\Delta G_{el} = \frac{E}{1-\nu}\varepsilon_V{}^2 V_m^{\alpha'} \tag{7}$$

where E represents Young's modulus, ν is Poisson's ratio, ε_V is the volumetric strain and $V_m^{\alpha'}$ is the molar volume of martensite. Here, the value of Young's modulus was taken as 219 GPa and the Poisson's ratio as 0.285, which were obtained by thermodynamic calculations using JMatPro software (version 12.4) [32].

The experimentally determined lattice parameters for the M50 steel were $a_\gamma = 3.570$ Å for austenite, $a_{\alpha'} = 2.840$ Å and $c_{\alpha'} = 2.897$ Å for martensite. The unit cell volume of austenite V_{cell}^{γ} is equal to $a_\gamma{}^3 = 4.55 \times 10^{-23}$ cm^3. Given the face-centred cubic (FCC) structure with 4 atoms per unit cell, the molar volume of austenite was derived as $V_m^{\gamma} = \frac{1}{4} N_A \bullet V_{cell}^{\gamma} = 6.85$ cm^3/mol, where N_A is Avogadro's number. Martensite, which has a BCT structure with 2 atoms per unit cell, exhibits a molar volume given by $V_m^{\alpha'} = \frac{1}{2} N_A \bullet V_{cell}^{\alpha'} = \frac{1}{2} N_A \bullet (a_{\alpha'}{}^2 c_{\alpha'}) =$

7.04 cm^3/mol. Therefore, the strain of volumetric deformation associated with the phase transformation was estimated as $\varepsilon_V = \frac{V_m^{\alpha'} - V_m^{\gamma}}{V_m^{\gamma}} = 0.027$. Based on these values, the resulting strain energy contribution of volume change ΔG_{el} in Eq.(7) was estimated to be 1572 J/mol.

Martensitic transformation kicks in only when the chemical driving force is sufficient to overcome the opposing non-chemical energy barriers. Fig. 8 presents the Gibbs free energies of martensite and austenite in M50 steel as a function of temperature, as obtained from Thermo-Calc 2024a with the TCFE13 database. The equilibrium temperature T_0 represents the critical point at which the Gibbs energy difference between austenite and martensite vanishes. The martensitic transformation initiates as soon as the temperature reaches a point where the chemical free energy change $\Delta G_T^{\gamma\to\alpha'}$, the difference in Gibbs free energies between austenite (γ) and martensite (α') at temperature T, is sufficient to counterbalance the elastic strain energy induced by the transformation. This defines the martensite start temperature (M_s), the point at which martensitic transformation is first observed during cooling. From Fig. 8, the critical driving force $\Delta G_{M_s}^{\gamma\to\alpha'}$ required to initiate transformation corresponds to 1572 J/mol, yielding an estimated M_s temperature of about 97 ℃.

Alternatively, M_s can be approximately estimated from the martensite phase fraction using the classical Koistinen and Marburger (K-M) equation [63]: $V_0 = 1 - \exp[-a(M_s - T_0)]$, where V_0 is the martensite volume fraction, a is the coefficient and T_0 is the final temperature to which the sample is cooled, approximately 300 K in this study. The martensite phase fraction in the fabricated M50 steel was determined to be 0.69 from the diffraction pattern acquired after manufacturing (Fig. 6a). The coefficient a is known to depend on steel chemical composition, especially carbon content [64]. In the absence of reported parameters for M50 steel, a value of a= 0.0122, reported for a Fe−0.8 C steel [65] with a comparable carbon content was used for the M_s estimation. Using the K-M relationship, the corresponding M_s temperature was estimated to be 123 ℃, which is slightly higher than the thermodynamically derived value of 97 ℃. The M_s temperature obtained from thermodynamic analysis is a model prediction based on the Gibbs free energy difference, whereas the K-M estimate is an empirical back-calculation based on the final martensite fraction at room temperature and a literature-derived coefficient. These two methods involve different assumptions. In particular, the coefficient a in K-M equation is material-dependent but no specific value has been reported for M50 steel, introducing additional uncertainty into the estimation. The thermodynamic prediction does not fully account for non-equilibrium segregation or complex thermal history inherent to LPBF. However, despite the slight difference, the two M_s values remain in reasonable agreement, supporting the reliability of both approaches in predicting the M_s temperature.

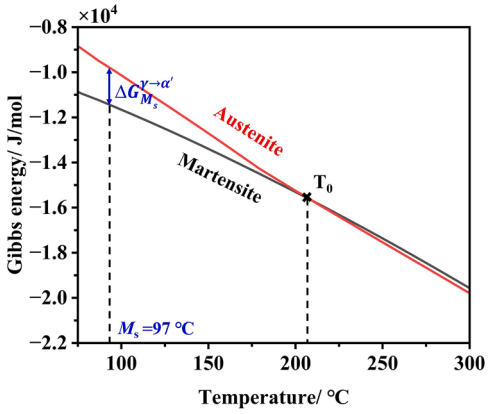

Fig. 8. Calculated Gibbs free energy (G) of austenite and martensite as a function of temperature for M50 steel.

Beyond thermodynamic considerations, chemical segregation during the rapid solidification inherent in the AM process must also be considered when analysing martensitic transformation behaviour. Previous studies reported that the microstructure of carbon-bearing alloyed steels produced by LPBF predominantly consists of solidification dendrites [1,4,5,8]. The enrichment of alloying elements in interdendritic regions stabilises austenite, making the martensitic transformation difficult [66]. Further, elemental segregation was reported to decrease M_s by up to 150 ℃ compared to the nominal composition due to the local enrichment of alloying elements in intercellular regions [3]. For M50 steel manufactured by LPBF with a columnar dendritic microstructure, the segregation of C, Cr, Mo, and V was observed at cell walls [67]. The segregation of alloying elements enhances the stability of retained austenite, thereby increasing the driving force required for transformation and lowering the M_s temperature. However, due to the complexity of chemical composition variations over the repeated thermal conditions, their effect on M_s temperature could not be evaluated here. Although this work does not provide a comprehensive temperature-dependent quantification of chemical effects, the results contribute valuable insights into the conditions for martensitic transformation in AM steels.

4.3. Stepwise martensitic transformation

The discrete steps observed at the start of Stage I, Stage II and Stage III, in Fig. 5c, where a substantial increase in martensite fraction occurred within a short duration, suggest that the transformation proceeded in abrupt bursts during cooling. The rapid martensitic transformation was considered a consequence of autocatalytic nucleation, occurring as long as the chemical driving force ($\Delta G^{\gamma\to\alpha'}$ in Fig. 8) is overcome [68,69]. Once the opposing strain and interfacial energies balance the chemical driving force, the transformation halts, requiring either further undercooling to increase the driving force or strain relaxation to enable continued transformation. The short plateau following each transformation step, such as the intervals from 375 to 400 ms and from 435 to 450 ms in Fig. 5c, may reflect a temporary reduction in the effective driving force for further martensitic transformation, which is probably a consequence of latent heat release during the phase transformation process [70]. If the heat generated by the phase transformation is not dissipated efficiently, the local temperature of the sample may temporarily stabilise or even increase slightly. Lee *et al.* [71] predicted that latent heat release during non-equilibrium martensitic transformation could contribute to an average temperature increase of about 43 ℃ in AISI 4340 steel. In addition, local stress accumulation associated with the volumetric and shear strains of newly formed martensite may also play an important role. Under LPBF conditions, transformation strains cannot be fully relaxed and may accumulate locally in the surrounding retained austenite and newly formed martensite, temporarily reducing the effective driving force for further martensitic transformation by mechanically stabilising the remaining austenite and impeding further martensitic transformation until sufficient cooling resumes.

It should be noted that although the LPBF melt track evolves dynamically during processing, transient thermal fluctuations associated with reheating occur mainly at the early stage, at approximately 170–200 ms. In contrast, martensitic transformation occurs at a later stage, first appearing at ~365 ms and continuing over a longer timescale. No evidence of partial remelting or reheating, such as pronounced peak shifting or reverse transformation, is observed during the martensitic transformation interval. Therefore, the observed stepwise behaviour is unlikely to be caused by local thermal fluctuations in the melt track.

Although the term 'stepwise martensitic transformation' has been used in previous literature, this phenomenon has typically been observed under different experimental conditions, often involving externally applied strains. For example, Hedström *et al.* [72] reported a

multiple-step martensitic transformation in AISI 301 stainless steel under applied strain during *in situ* tensile deformation, which represents a fundamentally different scenario from the rapid cooling conditions investigated in the present study. Similar mechanical strain-induced stepwise martensitic transformation has also been observed in other work [73,74]. By contrast, the stepwise martensitic transformation observed during LPBF is primarily cooling-induced, occurring after rapid solidification, although its progression may be modulated by transformation strain, residual stress and mechanical stabilisation of the remaining austenite. Previous studies have also reported multi-stage or discontinuous martensitic transformation kinetics in steels under cooling conditions. For example, Villa *et al.* [75] observed multi-stage martensite formation in ASIS 630 stainless steel during continuous cooling, with the transformation rate depending on the preceding cooling rate, which ranged from 1.5 to 50 ℃/min in their study. Loewy *et al.* [76] reported discontinuous transformation behaviour in maraging steel, where the transformation remained macroscopically athermal but the transformation rate evolved discontinuously as a series of rate maxima during continuous cooling. In these cases, autocatalytic nucleation was considered to contribute to the anomalous transformation behaviour.

Autocatalytic nucleation is widely recognised as the dominant mechanism driving martensitic transformation in low-carbon steels [77]. During martensitic transformation, dislocations were generated in the surrounding austenite by plastic deformation due to elastic strains, facilitating subsequent martensite nucleation. However, when the strain accumulated in retained austenite exceeds a critical value, further transformation is suppressed. This critical value of strain decreases with increasing carbon content in the retained austenite [78]. In high carbon steels, the significant solid solution strengthening effect of carbon plays a crucial role in stabilising austenite, impeding both interface motion and dislocation activity. Van Bohemen *et al.* [64,65] investigated the martensitic transformation progress in Fe−0.8 C plain carbon steels by dilatometry. They found that the carbon enrichment of the retained austenite not only suppressed the M_s temperature but also decelerated the transformation kinetics. This phenomenon was attributed to the mechanical stabilisation mechanism, which was identified to govern the kinetics of athermal martensitic transformation in carbon steels. The transformation is not primarily limited by nucleation but rather by the resistance of the austenite parent phase to the growth of martensite nuclei. In this study, the change in martensite tetragonality was delayed until after 500 ms (Fig. 6c), the point at which carbon content in martensite was sufficiently high to split the characteristic {200} diffraction peak. This suggests substantial carbon enrichment in the parent austenite phase. This time point corresponds to the final stage of Stage III in the transformation process, further supporting the interpretation that autocatalytic nucleation mechanisms dominate the two rapid abrupt bursts of transformation occurring between Stage I and Stage III. Meanwhile, mechanical stabilisation mechanisms became the dominant mechanism regulating the subsequent martensitic transformation from the austenite parent phase with higher carbon content.

The transformation observed in Stage IV (Fig. 5c) exhibits a more gradual and time-dependent transformation behaviour compared to the previous stages with a steady slope during the cooling process, indicating the martensitic transformation rate slowed significantly in the late period of the cooling process where the temperature and cooling rate were relatively low while the martensite fraction was high. The accumulated strain energy within the austenite induced by transformation counteracts the chemical driving force, thereby suppressing nucleation and reducing the transformation rate. The dependence of transformation on time and cooling rate suggests the involvement of a thermally activated mechanism, raising the possibility of thermally activated martensite growth and local strain relaxation in the austenite adjacent to newly formed martensite blocks. This interpretation aligns with the findings of Villa *et al.* [79] on stainless steel and Loewy *et al.* [76,80] on maraging steels, where the martensitic transformation rate was observed to decline at lower temperatures as the transformed fraction increased.

It should be noted that the phase fraction analysis assumes that the diffraction intensity is directly proportional to the phase fraction. This assumption has inherent limitations under LPBF conditions. Apart from the diffraction data, the phase fraction calculation performed in this study also depends on the structure factor and multiplicity factor, as shown in Eq. (2). These parameters were derived based on equilibrium crystallographic information and are unlikely to perfectly represent the true values under the non-equilibrium conditions of LPBF [81]. Without an experimental method to independently determine these parameters, particularly on the relevant timescales, such calculations inevitably require assumptions as adopted here. Therefore, the phase fractions derived from operando X-ray diffraction in this study are used primarily to track the relative temporal evolution of phase transformations, rather than to provide absolute phase fractions with the accuracy achievable through quantitative Rietveld refinement. In addition, the values obtained from the equation represent the phase fractions in the illuminated region, rather than the true bulk phase fractions in the sample, because the X-ray diffraction experiments were performed in reflection conditions.

Although theoretically martensite formation was expected to proceed in multiple stages during the cooling process, existing literature on stepwise martensitic transformation remains limited, with most studies focusing on stainless steels or maraging steels which are both low-carbon steels. In contrast, the M50 steel is a high-carbon high-alloy steel with a total alloying concentration of over 10 wt%. This work aims to provide the first insight into stepwise martensitic transformation behaviour in LPBF steels. The phenomenon was consistently observed across all samples, although the number and duration of the distinct transformation stages varied with processing condition. Nevertheless, a definitive conclusion about the martensitic transformation kinetics cannot be established solely from the present findings. Further investigation is required and is currently ongoing to elucidate the underlying transformation mechanisms.

5. Conclusions

The phase evolution of M50 steel during the LPBF process was monitored using operando X-ray diffraction, through which the stepwise martensitic transformation was observed for the first time under LPBF manufacturing conditions. By analysing the thermal conditions and evaluating the effect of input energy density on phase transformation, the following conclusions can be reached:

1. Austenite emerged as the primary phase during liquid solidification, subsequently transforming into martensite with approximately 20% retained austenite after LPBF manufacturing. The anticipated formation of δ-Fe and carbides, as predicted by thermodynamic calculations, was suppressed under high cooling rates.
2. The determined cooling rate of the solidification process was in the order of 10^5 ℃/s. It appeared to be minimally affected by variations in input energy density.
3. The carbon content in martensite increased from 0.58 to 0.68 wt%, accompanied by a rise in the c/a ratio from 1.018 to 1.021. Samples subjected to lower energy densities exhibited higher carbon content after manufacturing.
4. The observed staged increases in martensite phase fraction reveal a distinct stepwise transformation behaviour in M50 tool steel during rapid solidification and fast cooling of the LPBF process. The early abrupt transformations are likely governed by an autocatalytic nucleation mechanism. In contrast, the latter, more gradual transformation is attributed to mechanical stabilisation effects.

CRediT authorship contribution statement

Huayue Zhang: Writing – original draft, Methodology, Investigation, Conceptualization. **Andaç Özsoy:** Writing – review & editing, Investigation. **Gowtham Soundarapandiyan:** Writing – review & editing, Investigation. **Malgorzata Grazyna Makowska:** Writing – review & editing, Investigation. **Pedro E.J. Rivera-Diaz-del-Castillo:** Writing – review & editing, Resources. **Steven Van Petegem:** Writing – review & editing, Resources, Investigation, Data curation. **Bo Chen:** Writing – review & editing, Supervision, Funding acquisition, Conceptualization.

Declaration of Competing Interest

The authors declare that they have no known competing financial interests or personal relationships that could have appeared to influence the work reported in this paper.

Acknowledgements

This work was supported by the UK Engineering and Physical Sciences Research Council (EP/P025978/1 and EP/R043973/1). The work was carried out while H.Z. was undertaking her PhD under the supervision of B.C. at the University of Leicester. Her PhD scholarship jointly funded by the China Scholarship Council (CSC; No. 202006020022) and the College of Science and Engineering, University of Leicester. H.Z. and B.C. acknowledge Prof. Hui Peng and Dr Runqi Gao at Beihang University for donating M50 steel powder. We gratefully acknowledge the Paul Scherrer Institute (PSI) for awarding synchrotron beamtime in using beamline microXAS (Proposal ID: 20220055). S.V.P. and A.Ö. acknowledge financial support from the MULTIMAT project, funded by the ETH Board. G.S. and S.V.P. express gratitude for the financial support received from the PSI Cross Grant, "Enabling acoustic emission for monitoring selective laser melting guided by in situ synchrotron X-ray diffraction experiments.".

Appendix A. Diffraction patterns and derived phase fractions for all samples

Fig. A illustrates the evolution of diffraction patterns and phase fraction evolution as a function of time for all other samples. Despite variations in manufacturing parameters, all diffraction maps exhibit similar characteristic processes: thermal expansion-induced peak shifts to lower angles during heating, subsequent reversal upon cooling, and the onset of martensitic transformation at lower temperatures with prolonged cooling time. The stepwise martensitic transformation (described in Section 3.2) can be observed across all samples, corroborated by changes in martensite peak intensity within the corresponding diffraction map. Although the signal-to-noise ratio varies among the curves and the number of transformation steps differs under different conditions, the overall transformation trend remains evident.

For clarity, black dashed lines are added to each plot to delineate the transformation curve into several regions: early stages characterised by abrupt martensitic transformation and a later stage exhibiting a more gradual transformation behaviour. The wave-like fluctuations in the phase fraction, e.g., between 700 and 800 ms in Fig. Af, are attributed to oscillations in the incident X-ray beam energy during the beamtime session. The duration of each martensitic transformation stage and the final martensite fraction vary with different manufacturing conditions, highlighting the influence of LPBF processing parameters. A more detailed investigation into their effects on martensitic transformation in AM steels will be conducted in future studies.

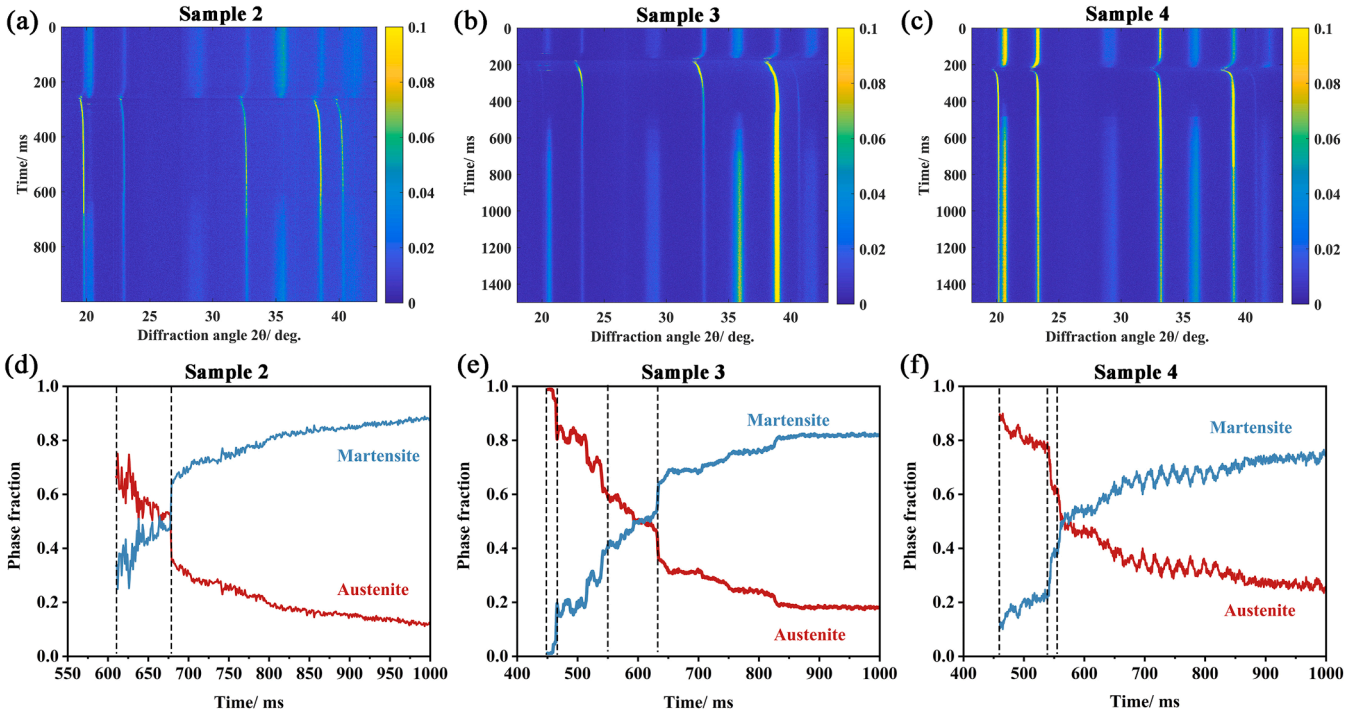

Figure A. (a)-(c) Evolution of diffraction patterns as a function of time measured by the X-ray beam on the surface layer during laser manufacturing, and (d)-(f) phase fraction evolution of austenite and martensite as a function of time for all samples: (a, d) Sample 2 (E_v=104.17 J•mm^{-3}); (b, e) Sample 3 (E_v=200 J•mm^{-3}); and (c, f) Sample 4 (E_v=277.78 J•mm^{-3})

Appendix B. Sensitivity analysis of the cooling rate determined from operando X-ray measurements

The temperature estimation was performed using a constant CTE value of 2.25 × 10^{-5} °C^{-1}, corresponding to 1420 °C, where the liquid phase is

predicted to start transforming into austenite. In reality, the CTE is temperature-dependent. A recalculation of the temperature was attempted by considering the temperature dependence of CTE.

Fig. Ba presents the linear expansion as a function of temperature, derived from the CTE values of M50 steel calculated by JMatPro, together with a fifth-order polynomial fit to the relationship between linear expansion and temperature (R^2=0.9999). Using the polynomial CTE, the estimated temperature is higher than that obtained using the constant CTE, as shown in Fig. Bb. This is expected because the constant CTE value was selected at 1420℃, a relatively high temperature, leading to an underestimation of the absolute temperature. Comparison of the temperature profiles obtained using the constant and polynomial CTE approaches shows a difference of ~200℃ within the analysed temperature range. However, the temperature shifts remain self-consistent, indicating that the slopes of the temperature profiles are largely preserved. This confirms that the calculated cooling rates are not significantly influenced by the choice between a constant and a temperature-dependent CTE.

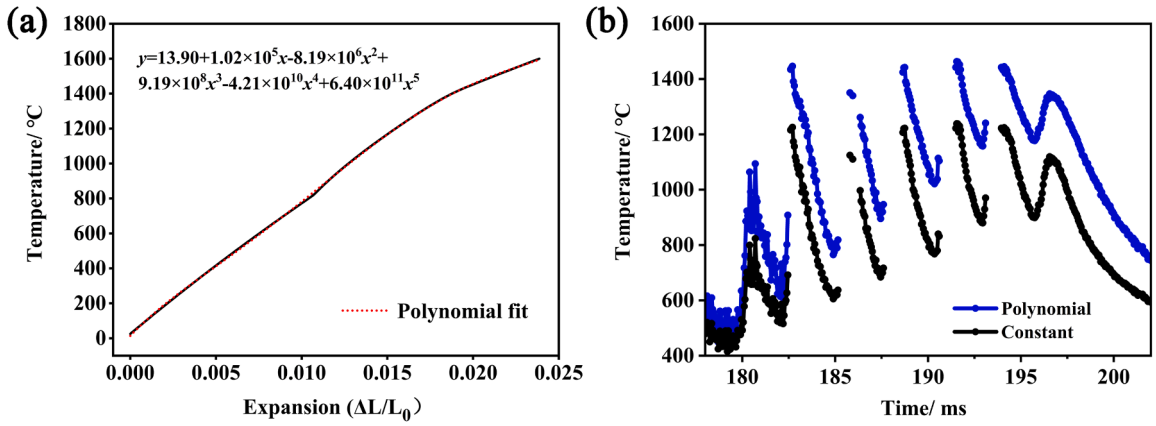

Figure B. (a) Fifth-order polynomial fit to linear expansion as a function of temperature; (b) comparison of temperature profiles estimated using constant CTE (black) and polynomial CTE (blue)

Data availability

Data will be made available on request.

References

[1] R. Mertens, B. Vrancken, N. Holmstock, Y. Kinds, J.P. Kruth, J. Van Humbeeck, Influence of powder bed preheating on microstructure and mechanical properties of H13 tool steel SLM parts, Phys. Procedia 83 (2016) 882–890, https://doi.org/10.1016/j.phpro.2016.08.092.

[2] M. Badrossamay, T.H.C. Childs, Further studies in selective laser melting of stainless and tool steel powders, Int. J. Mach. Tools Manuf. 47 (5) (2007) 779–784, https://doi.org/10.1016/j.ijmachtools.2006.09.013.

[3] C.-Y. Chou, N.H. Pettersson, A. Durga, F. Zhang, C. Oikonomou, A. Borgenstam, J. Odqvist, G. Lindwall, Influence of solidification structure on austenite to martensite transformation in additively manufactured hot-work tool steels, Acta Mater. 215 (2021) 117044, https://doi.org/10.1016/j.actamat.2021.117044.

[4] J. Saewe, N. Carstensen, P. Kürnsteiner, E.A. Jägle, J.H. Schleifenbaum, Influence of increased carbon content on the processability of high-speed steel HS6-5-3-8 by laser powder bed fusion, Addit. Manuf. 46 (2021) 102125, https://doi.org/10.1016/j.addma.2021.102125.

[5] K. Geenen, A. Röttger, F. Feld, W. Theisen, Microstructure, mechanical, and tribological properties of M3:2 high-speed steel processed by selective laser melting, hot-isostatic pressing, and casting, Addit. Manuf. 28 (2019) 585–599, https://doi.org/10.1016/j.addma.2019.05.028.

[6] J. Saewe, C. Gayer, A. Vogelpoth, J.H. Schleifenbaum, Feasability investigation for laser powder bed fusion of high-speed steel AISI M50 with base preheating system, BHM Berg. - und H. üttenmännische Mon. 164 (3) (2019) 101–107, https://doi.org/10.1007/s00501-019-0828-y.

[7] S. Qin, J. Saewe, J. Kunz, S. Herzog, A. Kaletsch, J.H. Schleifenbaum, C. Broeckmann, Influence of Preheating Temperature on Microstructure Evolution and Hardness of High-Speed Steel AISI M50 Processed by Laser Powder Bed Fusion, Steel Res. Int. 94 (6) (2023) 2200784, https://doi.org/10.1002/srin.202200784.

[8] J. Kunz, J. Saewe, S. Herzog, A. Kaletsch, J.H. Schleifenbaum, C. Broeckmann, Mechanical properties of high-speed steel AISI M50 produced by laser powder bed fusion, Steel Res. Int. 91 (5) (2020) 1900562, https://doi.org/10.1002/srin.201900562.

[9] G. Guetard, I. Toda-Caraballo, P.E.J. Rivera-Díaz-del-Castillo, Damage evolution around primary carbides under rolling contact fatigue in VIM–VAR M50, Int. J. Fatigue 91 (2016) 59–67, https://doi.org/10.1016/j.ijfatigue.2016.05.026.

[10] K. Kempen, B. Vrancken, S. Buls, L. Thijs, J. Van Humbeeck, J.-P. Kruth, Selective laser melting of crack-free high density M2 high speed steel parts by baseplate preheating, J. Manuf. Sci. Eng. 136 (6) (2014), https://doi.org/10.1115/1.4028513.

[11] Y. Yin, Q. Tan, M. Bermingham, N. Mo, J. Zhang, M.-X. Zhang, Laser additive manufacturing of steels, Int. Mater. Rev. (2021) 1–87, https://doi.org/10.1080/09506608.2021.1983351.

[12] S.J. Donachie, G.S. Ansell, The effect of quench rate on the properties and morphology of ferrous martensite, Metall. Trans. A 6 (10) (1975) 1863, https://doi.org/10.1007/BF02646850.

[13] G.S. Ansell, S.J. Donachie, R.W. Messler, The effect of quench rate on the martensitic transformation in Fe−C alloys, Metall. Trans. 2 (9) (1971) 2443–2449, https://doi.org/10.1007/BF02814881.

[14] J. Wang, H. Li, M.W. Fu, The typical cellular microstructures developed in powder-based additively manufactured metallic materials: formation mechanisms, properties, outlooks and challenges, Int. J. Mach. Tools Manuf. 212 (2025) 104332, https://doi.org/10.1016/j.ijmachtools.2025.104332.

[15] H.-S. Yang, H.K.D.H. Bhadeshia, Austenite grain size and the martensite-start temperature, Scr. Mater. 60 (7) (2009) 493–495, https://doi.org/10.1016/j.scriptamat.2008.11.043.

[16] M. Hunkel, Tempering effects of athermal martensite during quenching and reheating of a SAE 52100 bearing steel, Mater. Sci. Eng. A 790 (2020) 139601, https://doi.org/10.1016/j.msea.2020.139601.

[17] Y. Bai, Y.J. Lee, Y. Guo, Q. Yan, C. Zhao, A.S. Kumar, J.M. Xue, H. Wang, Efficient post-processing of additive manufactured maraging steel enhanced by the mechanochemical effect, Int. J. Mach. Tools Manuf. 193 (2023) 104086, https://doi.org/10.1016/j.ijmachtools.2023.104086.

[18] L. Wang, Q. Guo, L. Chen, W. Yan, In-situ experimental and high-fidelity modeling tools to advance understanding of metal additive manufacturing, Int. J. Mach. Tools Manuf. 193 (2023) 104077, https://doi.org/10.1016/j.ijmachtools.2023.104077.

[19] S. Hocine, H. Van Swygenhoven, S. Van Petegem, C.S.T. Chang, T. Maimaitiyili, G. Tinti, D. Ferreira Sanchez, D. Grolimund, N. Casati, Operando X-ray diffraction during laser 3D printing, Mater. Today 34 (2020) 30–40, https://doi.org/10.1016/j.mattod.2019.10.001.

[20] M. Chen, S. Van Petegem, Z. Zou, M. Simonelli, Y.Y. Tse, C.S.T. Chang, M. G. Makowska, D. Ferreira Sanchez, H. Moens-Van Swygenhoven, Microstructural engineering of a dual-phase Ti-Al-V-Fe alloy via in situ alloying during laser powder bed fusion, Addit. Manuf. 59 (2022) 103173, https://doi.org/10.1016/j.addma.2022.103173.

[21] J.A. Glerum, S. Hocine, C.S.T. Chang, C. Kenel, S. Van Petegem, N. Casati, D. F. Sanchez, H. Van Swygenhoven, D.C. Dunand, Operando X-ray diffraction study of thermal and phase evolution during laser powder bed fusion of Al-Sc-Zr elemental powder blends, Addit. Manuf. 55 (2022) 102806, https://doi.org/10.1016/j.addma.2022.102806.

[22] H.-H. König, N.H. Pettersson, A. Durga, S. Van Petegem, D. Grolimund, A. C. Chuang, Q. Guo, L. Chen, C. Oikonomou, F. Zhang, G. Lindwall, Solidification modes during additive manufacturing of steel revealed by high-speed X-ray diffraction, Acta Mater. 246 (2023) 118713, https://doi.org/10.1016/j.actamat.2023.118713.

[23] J. Epp, J. Dong, H. Meyer, A. Bohlen, Analysis of cyclic phase transformations during additive manufacturing of hardenable tool steel by in-situ X-ray diffraction

experiments, Scr. Mater. 177 (2020) 27–31, https://doi.org/10.1016/j.scriptamat.2019.09.021.
[24] A.Cd.F. Silveira, R. Fechte-Heinen, J. Epp, Microstructure evolution during laser-directed energy deposition of tool steel by in situ synchrotron X-ray diffraction, Addit. Manuf. 63 (2023) 103408, https://doi.org/10.1016/j.addma.2023.103408.
[25] L. Gao, Y. Chen, X. Zhang, S.R. Agnew, A.C. Chuang, T. Sun, Evolution of dislocations during the rapid solidification in additive manufacturing, Nat. Commun. 16 (1) (2025) 4696, https://doi.org/10.1038/s41467-025-59988-5.
[26] ASTM A600-92a(2016), Standard Specification for Tool Steel High Speed, ASTM International, West Conshohocken, PA, 2016.
[27] G. Ashiotis, A. Deschildre, Z. Nawaz, J.P. Wright, D. Karkoulis, F.E. Picca, J. Kieffer, The fast azimuthal integration Python library: pyFAI, J. Appl. Crystallogr. 48 (2) (2015) 510–519, https://doi.org/10.1107/S1600576715004306.
[28] S. Hocine, S. Van Petegem, U. Frommherz, G. Tinti, N. Casati, D. Grolimund, H. Van Swygenhoven, A miniaturized selective laser melting device for operando X-ray diffraction studies, Addit. Manuf. 34 (2020) 101194, https://doi.org/10.1016/j.addma.2020.101194.
[29] S. Harjo, N. Tsuchida, J. Abe, W. Gong, Martensite phase stress and the strengthening mechanism in TRIP steel by neutron diffraction, Sci. Rep. 7 (1) (2017) 15149, https://doi.org/10.1038/s41598-017-15252-5.
[30] S. Harjo, J. Abe, K. Aizawa, W. Gong, T. Iwahashi, Deformation behavior of an austenitic steel by neutron diffraction, Proc. 12th Asia Pac. Phys. Conf. (APPC12) (2014) 014017.
[31] S. Hocine, H. Van Swygenhoven, S. Van Petegem, Verification of selective laser melting heat source models with operando X-ray diffraction data, Addit. Manuf. 37 (2021) 101747, https://doi.org/10.1016/j.addma.2020.101747.
[32] N. Saunders, U. Guo, X. Li, A. Miodownik, J.-P. Schillé, Using JMatPro to model materials properties and behavior, Jom 55 (12) (2003) 60–65.
[33] B.D. Cullity, Elements of X-ray Diffraction, third ed, Addison-Wesley Publishing, 1956.
[34] R. Seede, D. Shoukr, B. Zhang, A. Whitt, S. Gibbons, P. Flater, A. Elwany, R. Arroyave, I. Karaman, An ultra-high strength martensitic steel fabricated using selective laser melting additive manufacturing: Densification, microstructure, and mechanical properties, Acta Mater. 186 (2020) 199–214, https://doi.org/10.1016/j.actamat.2019.12.037.
[35] P.A. Hooper, Melt pool temperature and cooling rates in laser powder bed fusion, Addit. Manuf. 22 (2018) 548–559, https://doi.org/10.1016/j.addma.2018.05.032.
[36] N. Seljakow, J. Kurdjmoff, N. Goodtzov, Tetragonal Structure of Carbon Steel, 494-494, Nature 119 (2996) (1927), https://doi.org/10.1038/119494a0.
[37] H. Bhadeshia, R. Honeycombe, Steels: microstructure and properties, Butter -Heinemann (2017).
[38] Y. Lu, H. Yu, R.D. Sisson, The effect of carbon content on the c/a ratio of as-quenched martensite in Fe-C alloys, Mater. Sci. Eng. A 700 (2017) 592–597, https://doi.org/10.1016/j.msea.2017.05.094.
[39] T. Masumura, K. Inami, K. Matsuda, T. Tsuchiyama, S. Nanba, A. Kitahara, Quantitative evaluation of dislocation density in as-quenched martensite with tetragonality by X-ray line profile analysis in a medium-carbon steel, Acta Mater. 234 (2022) 118052, https://doi.org/10.1016/j.actamat.2022.118052.
[40] L. Xiao, Z. Fan, Z. Jinxiu, Z. Mingxing, K. Mokuang, G. Zhenqi, Lattice-parameter variation with carbon content of martensite. I. X-ray-diffraction experimental study, Phys. Rev. B 52 (14) (1995) 9970–9978, https://doi.org/10.1103/PhysRevB.52.9970.
[41] O.D. Sherby, J. Wadsworth, D.R. Lesuer, C.K. Syn, Revisiting the Structure of Martensite in Iron-Carbon Steels, Mater. Trans. 49 (9) (2008) 2016–2027, https://doi.org/10.2320/matertrans.MRA2007338.
[42] G.B. Olson, M. Cohen, A general mechanism of martensitic nucleation: Part I. General concepts and the FCC → HCP transformation, Metall. Trans. A 7 (12) (1976) 1897–1904, https://doi.org/10.1007/BF02659822.
[43] S. Mahajan, M.L. Green, D. Brasen, A model for the FCC→HCP transformation, its applications, and experimental evidence, Metall. Trans. A 8 (2) (1977) 283–293, https://doi.org/10.1007/BF02661642.
[44] T. Tanaka, N. Maruyama, N. Nakamura, A.J. Wilkinson, Tetragonality of Fe-C martensite – a pattern matching electron backscatter diffraction analysis compared to X-ray diffraction, Acta Mater. 195 (2020) 728–738, https://doi.org/10.1016/j.actamat.2020.06.017.
[45] L. Thijs, K. Kempen, J.-P. Kruth, J. Van Humbeeck, Fine-structured aluminium products with controllable texture by selective laser melting of pre-alloyed AlSi10Mg powder, Acta Mater. 61 (5) (2013) 1809–1819, https://doi.org/10.1016/j.actamat.2012.11.052.
[46] J.W. Elmer, S.M. Allen, T.W. Eagar, Microstructural development during solidification of stainless steel alloys, Metall. Trans. A 20 (10) (1989) 2117–2131, https://doi.org/10.1007/BF02650298.
[47] G.T. Gray, V. Livescu, P.A. Rigg, C.P. Trujillo, C.M. Cady, S.R. Chen, J.S. Carpenter, T.J. Lienert, S.J. Fensin, Structure/property (constitutive and spallation response) of additively manufactured 316L stainless steel, Acta Mater. 138 (2017) 140–149, https://doi.org/10.1016/j.actamat.2017.07.045.
[48] T. DebRoy, H.L. Wei, J.S. Zuback, T. Mukherjee, J.W. Elmer, J.O. Milewski, A. M. Beese, A. Wilson-Heid, A. De, W. Zhang, Additive manufacturing of metallic components – process, structure and properties, Progress. Mater. Sci. 92 (2018) 112–224, https://doi.org/10.1016/j.pmatsci.2017.10.001.
[49] J. Saewe, M.B. Wilms, J. Lucas, J.H. Schleifenbaum, Influence of Preheating Temperature on Hardness and Microstructure of High-Speed Steel HS6-5-3-8 Manufactured by Laser Powder Bed Fusion, Metal Additive Manufacturing Conference (MAMC): Örebro, Sweden, 2019.
[50] C. Botero, M. Ramsperger, A. Selte, K. Åsvik, A. Koptyug, P. Skoglund, S. Roos, L.-E. Rännar, M. Bäckström, Additive manufacturing of a cold-work tool steel using electron beam melting, Steel Res. Int. 91 (5) (2020) 1900448, https://doi.org/10.1002/srin.201900448.
[51] J. Jin, R. Gao, H. Peng, H. Guo, S. Gong, B. Chen, Rapid solidification microstructure and carbide precipitation behavior in electron beam melted high-speed steel, Metall. Mater. Trans. A 51 (5) (2020) 2411–2429, https://doi.org/10.1007/s11661-020-05661-z.
[52] J. Boes, A. Röttger, W. Theisen, C. Cui, V. Uhlenwinkel, A. Schulz, H.W. Zoch, F. Stern, J. Tenkamp, F. Walther, Gas atomization and laser additive manufacturing of nitrogen-alloyed martensitic stainless steel, Addit. Manuf. 34 (2020) 101379, https://doi.org/10.1016/j.addma.2020.101379.
[53] L.-E. Rännar, A. Koptyug, J. Olsén, K. Saeidi, Z. Shen, Hierarchical structures of stainless steel 316L manufactured by Electron Beam Melting, Addit. Manuf. 17 (2017) 106–112, https://doi.org/10.1016/j.addma.2017.07.003.
[54] R. Lehnert, R. Wagner, C. Burkhardt, P. Clausnitzer, A. Weidner, M. Wendler, O. Volkova, H. Biermann, Microstructural and mechanical characterization of high-alloy quenching and partitioning TRIP steel manufactured by electron beam melting, Mater. Sci. Eng. A 794 (2020) 139684, https://doi.org/10.1016/j.msea.2020.139684.
[55] P. Kürnsteiner, M.B. Wilms, A. Weisheit, P. Barriobero-Vila, E.A. Jägle, D. Raabe, Massive nanoprecipitation in an Fe-19Ni-xAl maraging steel triggered by the intrinsic heat treatment during laser metal deposition, Acta Mater. 129 (2017) 52–60, https://doi.org/10.1016/j.actamat.2017.02.069.
[56] N. Du, H. Liu, Y. Cao, P. Fu, C. Sun, H. Liu, D. Li, Formation mechanism of MC and M2C primary carbides in as-cast M50 bearing steel, Mater. Charact. 174 (2021) 111011, https://doi.org/10.1016/j.matchar.2021.111011.
[57] S.E. Hopkin, M. Danaie, G. Guetard, P. Rivera-Diaz-del-Castillo, P.A.J. Bagot, M. P. Moody, Correlative atomic scale characterisation of secondary carbides in M50 bearing steel, Philos. Mag. 98 (9) (2018) 766–782, https://doi.org/10.1080/14786435.2017.1410290.
[58] J.E. Bridge, G.N. Maniar, T.V. Philip, Carbides in M50 high speed steel, Metallurgical and, Mater. Trans. B 2 (8) (1971) 2209–2214, https://doi.org/10.1007/BF02917552.
[59] C. Nunes, A. Mahendrasingam, R. Suryanarayanan, Quantification of Crystallinity in Substantially Amorphous Materials by Synchrotron X-ray Powder Diffractometry, Pharm. Res. 22 (11) (2005) 1942–1953, https://doi.org/10.1007/s11095-005-7626-9.
[60] B. Ahmad, S.O. van der Veen, M.E. Fitzpatrick, H. Guo, Residual stress evaluation in selective-laser-melting additively manufactured titanium (Ti-6Al-4V) and inconel 718 using the contour method and numerical simulation, Addit. Manuf. 22 (2018) 571–582, https://doi.org/10.1016/j.addma.2018.06.002.
[61] R.W. Cahn, P. Haasen. Physical metallurgy, fourth ed., Elsevier, Amsterdam, 1996.
[62] H. Bhadeshia. Theory of Transformations in Steels, 1st ed., CRC Press, 2021.
[63] D.P. Koistinen, R.E. Marburger, A general equation prescribing the extent of the austenite-martensite transformation in pure iron-carbon alloys and plain carbon steels, Acta Metall. 7 (1) (1959) 59–60, https://doi.org/10.1016/0001-6160(59)90170-1.
[64] S.M.C. Van Bohemen, J. Sietsma, Martensite Formation in Partially and Fully Austenitic Plain Carbon Steels, Metall. Mater. Trans. A 40 (5) (2009) 1059–1068, https://doi.org/10.1007/s11661-009-9796-2.
[65] S.M.C. van Bohemen, J. Sietsma, Kinetics of martensite formation in plain carbon steels: Critical assessment of possible influence of austenite grain boundaries and autocatalysis, Mater. Sci. Technol. 30 (9) (2014) 1024–1033, https://doi.org/10.1179/1743284714Y.0000000532.
[66] M. Ohring, How engineering materials are strengthened and toughened, in: M. Ohring (Ed.), Engineering Materials Science, Academic Press, San Diego, 1995, pp. 431–500.
[67] S. Qin, S. Herzog, A. Kaletsch, C. Broeckmann, Effects of Pressure on Microstructure and Residual Stresses during Hot Isostatic Pressing Post Treatment of AISI M50 Produced by Laser Powder-Bed Fusion, Metals 11 (4) (2021) 596, https://doi.org/10.3390/met11040596.
[68] G.B. Olson, M. Cohen, Kinetics of strain-induced martensitic nucleation, Metall. Trans. A 6 (4) (1975) 791–795, https://doi.org/10.1007/BF02672301.
[69] Y.C. Liu, F. Sommer, E.J. Mittemeijer, Abnormal austenite–ferrite transformation behaviour in substitutional Fe-based alloys, Acta Mater. 51 (2) (2003) 507–519, https://doi.org/10.1016/S1359-6454(02)00434-2.
[70] J.R.C. Guimarães, J.C. Gomes, A metallographic study of the influence of the austenite grain size on martensite kinetics, Acta Metall. 26 (10) (1978) 1591–1596, https://doi.org/10.1016/0001-6160(78)90068-8.
[71] S.-J. Lee, Y.-K. Lee, Latent heat of martensitic transformation in a medium-carbon low-alloy steel, Scr. Mater. 60 (11) (2009) 1016–1019, https://doi.org/10.1016/j.scriptamat.2009.02.042.
[72] P. Hedström, U. Lienert, J. Almer, M. Odén, Stepwise transformation behavior of the strain-induced martensitic transformation in a metastable stainless steel, Scr. Mater. 56 (3) (2007) 213–216, https://doi.org/10.1016/j.scriptamat.2006.10.009.
[73] A.K. De, J.G. Speer, D.K. Matlock, D.C. Murdock, M.C. Mataya, R.J. Comstock, Deformation-induced phase transformation and strain hardening in type 304 austenitic stainless steel, Metall. Mater. Trans. A 37 (6) (2006) 1875–1886, https://doi.org/10.1007/s11661-006-0130-y.
[74] B. Sun, N. Vanderesse, F. Fazeli, C. Scott, J. Chen, P. Bocher, M. Jahazi, S. Yue, Discontinuous strain-induced martensite transformation related to the Portevin-Le Chatelier effect in a medium manganese steel, Scr. Mater. 133 (2017) 9–13, https://doi.org/10.1016/j.scriptamat.2017.01.022.

[75] M. Villa, K. Pantleon, M. Reich, O. Kessler, M.A.J. Somers, Kinetics of anomalous multi-step formation of lath martensite in steel, Acta Mater. 80 (2014) 468–477, https://doi.org/10.1016/j.actamat.2014.08.031.
[76] S. Loewy, B. Rheingans, S.R. Meka, E.J. Mittemeijer, Unusual martensite-formation kinetics in steels: Observation of discontinuous transformation rates, Acta Mater. 64 (2014) 93–99, https://doi.org/10.1016/j.actamat.2013.11.052.
[77] M. Cohen, Martensitic nucleation-revisited, Mater. Trans. JIM 33 (3) (1992) 178–183, https://doi.org/10.2320/matertrans1989.33.178.
[78] S. Chatterjee, H. Bhadeshia, Transformation induced plasticity assisted steels: stress or strain affected martensitic transformation? Mater. Sci. Technol. 23 (9) (2007) 1101–1104.
[79] M. Villa, M.F. Hansen, K. Pantleon, M.A.J. Somers, Thermally activated growth of lath martensite in Fe–Cr–Ni–Al stainless steel, Mater. Sci. Technol. 31 (1) (2015) 115–122, https://doi.org/10.1179/1743284714Y.0000000583.
[80] S. Loewy, B. Rheingans, S.R. Meka, E.J. Mittemeijer, Modulated martensite formation behavior in Fe–Ni-based alloys; athermal and thermally activated mechanisms, J. Mater. Res. 30 (13) (2015) 2101–2107, https://doi.org/10.1557/jmr.2015.175.
[81] D.M. Collins, D.J. Crudden, E. Alabort, T. Connolley, R.C. Reed, Time-resolved synchrotron diffractometry of phase transformations in high strength nickel-based superalloys, Acta Mater. 94 (2015) 244–256, https://doi.org/10.1016/j.actamat.2015.04.046.